Archives of Civil and Mechanical Engineering (2023) 23:80
https://doi.org/10.1007/s43452-022-00594-3

ORIGINAL ARTICLE

Effect of chromium doping on the structure and mechanical properties of anti-wear TiB_2 coatings

Łukasz Cieniek[1] · Edyta Chudzik-Poliszak[1] · Tomasz Moskalewicz[1] · Agnieszka Kopia[1] · Jerzy Smolik[2]

Received: 15 September 2022 / Revised: 1 December 2022 / Accepted: 24 December 2022 / Published online: 15 February 2023

Abstract

TiB_2-based coatings have been intensively developed due to their physical and mechanical properties, including excellent thermal stability and high hardness with good abrasion and corrosion resistance, which appear to be the most beneficial in industrial application. Previous investigations have shown that doping TiB_2 with W, Ni and C can significantly reduce residual stresses and improve adhesion, making these coatings ideal on tools to machining aluminum alloys. The aim of this study was to analyze the effect of an Cr interlayer on the durability (adhesion) of the fabricated $Ti_{1-x}Cr_xB_2$ ($x = 0$; 0.03; 0.06; 0.10) films and determine the influence of Cr on their microstructure and mechanical properties. The structural characterization of $Ti_{1-x}Cr_xB_2$ coatings was carried out using X-ray diffraction, X-ray photoelectron spectroscopy, transmission electron microscopy and atomic force microscopy. To investigate the mechanical properties, nano-scratch and—hardness tests (NST, NHT) were performed, and fracture toughness of the substrate layer systems was determined. The use of an adhesive layer of pure Cr increased the adhesion of the coatings to the substrate. It is shown that the changes in Cr content not only affect the microstructure, mainly by decreasing the crystallite size (column width), but also the texture (preferred film orientation) and phase composition. The addition of chromium also has an effect on the mechanical properties of TiB_2 films by reducing their hardness and Young's modulus and increasing their fracture toughness (K_{IC}).

1 Introduction

The dynamic development of materials engineering techniques in the field of surface coatings deposition processes for tool components makes it necessary to search for the simplest solutions (structures and compositions) ensuring stable and reliable operation for the longest possible time. Such a trend is clearly observed in the production of anti-wear coatings dedicated for common machining, but also for use in automotive industries [1], gas turbines [2] and metal-cutting tools [3]. Among commonly used hard anti-wear coatings, TiN still holds a dominant industrial position, although its adhesion to metallic substrates is frequently shown to be weaker than for borides and carbides [4]. Nevertheless, nitrides have been regarded as more promising in this respect as they are softer and more ductile than borohydrides and carbides, with lower melting points, but higher chemical stability. Recently, new TiB_2-based coatings have been intensively developed due to their potential physical and mechanical properties, such as high melting point, low compressive residual stress state [5], good abrasion [6], increased hardness [7], corrosion resistance, high friction resistance [8] and excellent thermal stability. However, surface defects (droplets and nodular defects) observed on hard coatings [9] deposited on machining tools often serve as crack initiation sites in the substrate during operation, leading to complete failure of the entire tool. This is unacceptable for coating materials, especially those used in anti-wear systems. Therefore, ensuring a proper stress distribution, in addition to attaining high quality coatings, should be

✉ Łukasz Cieniek
lukasz.cieniek@agh.edu.pl

Edyta Chudzik-Poliszak
edytachudzik@gmail.com

Tomasz Moskalewicz
tomasz.moskalewicz@agh.edu.pl

Agnieszka Kopia
kopia@agh.edu.pl

Jerzy Smolik
jerzy.smolik@itee.lukasiewicz.gov.pl

1 Faculty of Metals Engineering and Industrial Computer Science, AGH University of Science and Technology, al. A. Mickiewicza 30, 30-059 Krakow, Poland

2 Łukasiewicz Research Network-Institute for Sustainable Technologies, K. Pułaskiego St. 6/10, 26-600 Radom, Poland

addressed. The best and simplest solution that significantly improves the adhesion of high-strength coatings and simultaneously relaxes the generated tensile stresses is the application of an interlayer as a transition zone. This solution is promising as it enables the consideration of coating materials that would otherwise be disqualified due to their stiffness and brittleness, while also significantly improving film-substrate adhesion [10]. Furthermore, it has been observed that the transition interlayer can divert or even stop discontinuities/cracks propagating through the coating. Although this may consequently lead to coating delamination, it protects the core/substrate under wear conditions. This mechanism is a principal approach used in the construction of layered composites [11]. High strength anti-wear coatings have been the subject of many studies over the past years [12]. They remain challenging and reveal interesting properties especially due to the use of different compositional configurations or changes in stoichiometry.

Ali et al. [13] deposited Ti as a sublayer for TiB_2–Al_2O_3 coatings to enhance the adherence between the coating and the substrate and also to increase the Young' modulus.

The effect of nitriding an H13 steel substrate on the hardness and adhesion properties of TiB_2 coatings was analyzed by Park et al. [14]. After the process, an Fe_4N phase was identified in the steel substrate. Such surface treatment noticeably improved the adhesion of TiB_2 coatings (increase to ~30 N). Ozkan [15] described the friction and wear enhancement of magnetron sputtered bilayer Cr–N/TiB_2 coatings. He showed that combined bilayer ceramic and metallic coatings can be used in mechanical systems such as the moving parts of an internal combustion engine as lubricated conditions to improve the tribological behaviors of the steel surfaces.

A bilayer coating of ~ 3.4 µm thickness, consisting of a nanocrystalline TiB_2 protective top layer and a TiN diffusion-barrier bottom layer deposited by chemical vapor deposition (CVD) method, was analyzed by Gruber et al. [16]. They used a TiN coating to primarily serve as a barrier against B diffusion into the substrate, which would otherwise compromise coating adhesion to cemented carbide cutting tools. The coating TiN succeeded in this role.

Besides the adhesion to the substrate, the next problem in TiB_2 coating is the low cracking resistance. These properties can be altered by the addition of certain elements to the TiB_2 structure. In the literature, the authors proposed a Ti–B–M system where M = Ni, Cr, Zr, C, W. A TiB_2 coating with 0–12.6 at% Ni contents was deposited using the magnetron sputtering (MS) method by Wang et al. [17]. They demonstrated that additions of Ni to form the cemented boride nanostructure could noticeably toughen the TiB_2 coatings. E. Contreras et al. [18] analyzed the TiB_2 coatings with doping of carbon. The doping of carbon in the TiB_2 led to a progressive reduction in the hardness and Young's modulus. In our previous work [19], we presented that an addition of tungsten to a TiB_2 coating produced by MS had a considerable impact on the microstructure and increased the brittle cracking resistance.

Several classic chemical vapor deposition (CVD) [20] and vapor assisted techniques [21], including physical vapor deposition (PVD) [22], are used to deposit TiB_2 coatings. However, one of the most versatile deposition methods remains magnetron sputtering (MS) [23], which allows precise control of the ion bombardment conditions during growth, thus enabling extensive modification and improvement of coating properties [24]. Conducting the deposition process under low temperature conditions, as done in the physical vapor deposition (PVD) method, produces TiB_2 coatings that show great potential in tribological applications.

This paper discusses the structural changes, chemical and phase composition differences, and analyzes the mechanical properties of Cr-doped TiB_2 coatings. A magnetron sputtering method was proposed for the deposition of $Ti_{1-x}Cr_xB_2$ coatings on steel substrates. The deposition parameters were optimized based on our previous studies [7]. To change the residual stress and increase the adhesion of the TiB_2 coating to the substrate, we used a Cr transition metal coating as a sublayer. To reduce or eliminate the problem of low fracture toughness, it was proposed to fabricate and analyze coatings with several variants of Cr doping concentration: $Ti_{1-x}Cr_xB_2$ (x = 0; 0.03; 0.06; 0.1).

2 Experimental methods

2.1 Coating fabrication

$Ti_{1-x}Cr_xB_2$ coatings with different chromium content x = 0; 0.03; 0.06; 0.1 were deposited by means of direct current magnetron sputtering (DCMS) at the Łukasiewicz Research Network-Institute for Sustainable Technology in Radom (Poland). A Twin direct current (DC) magnetron setup was used, equipped with disc-shaped targets made of pure chromium (Cr, ∅140 mm) and titanium diboride (TiB_2, ∅ 100 mm), both fixed on copper pads. The substrates were made from W320 hot worked steel, tempered to 50 ÷ 52 HRC. Before the deposition process, the substrates were thoroughly washed with pure alcohol and etched with argon ions (voltage of − 800 V) to remove surface impurities. During deposition, the argon pressure in the vacuum chamber was 4×10^{-3} mbar, and the substrate bias − 100 V was applied. The power on the Cr target was varied in the range of 70 ÷ 165 W to attain various Cr concentrations, whereas the power on the TiB_2 target was held constant at 2000 W. The deposition time of each coating was 40 min. Their thicknesses were in the range of 1.2 ÷ 1.8 µm depending on the Cr content.

2.2 Coatings characterization

The microstructure of the $Ti_{1-x}Cr_xB_2$ coatings was investigated by means of transmission electron microscopy (TEM, model JEOL JEM-2010ARP, 200 kV) by preparing cross-sectional lamella manufactured via focused ion beam (FIB). Selected area electron diffraction (SAED) patterns, obtained using an ∅ 150 nm aperture, were used for phase analysis. They were interpreted using JEMS software (P. Stadelmann, Switzerland). Phase identification was facilitated using the identified inorganic crystal structures database ICSD (FIZ Karlsruhe, Germany) [25].

Phase analyses of the coatings were performed by means of grazing incidence X-ray diffraction (GI-XRD) using a PANanalytical EMPYREAN DY 1061 diffractometer equipped with a Cu Kα lamp (0.154 nm), at an angle of 3°. The effective penetration depth was determined for GRAZING using Eq. (1) [26]:

$$Z = \frac{-\ln(1 - Gx)}{\mu\left[\frac{1}{\sin\alpha} + \frac{1}{\sin(2\theta-\alpha)}\right]} \tag{1}$$

where G_x is the fraction of the incident beam absorbed by the material before the beam reaches the maximum penetration depth Z (nm), μ is the linear attenuation coefficient of the material, α is the incidence angle (°) and 2θ is the angle of the diffracted beam (°).

X-ray diffraction patterns were fitted using Highscore Plus software and crystallographic information files (CIF). Crystallite sizes D (nm) were determined using Scherrer's equation Eq. (2) [27]:

$$D = \frac{K \cdot \lambda}{\beta \cdot \cos\Theta} \tag{2}$$

where K is a dimensionless shape factor, with a value close to unity, λ is the wavelength of X-ray source (nm), β is full width at half maximum (rad), θ is the diffracted angle (°).

X-ray photoelectron spectroscopy (XPS) was used to determine the chemical states of the elements in the coatings using a PHI5000 Versa Probe II instrument equipped with a surface charge analyzer (SCA). The monochromatic Al Kα source worked at 15 kV. Argon was used as the protective gas.

The surface topography of the coatings was analyzed via atomic force microscopy (AFM, model Veeco Dimension Icon SPM) with a NanoScopeV controller.

The hardness of Cr-doped TiB_2 coatings deposited on W320 steel substrates was investigated by nanoindentation using a CSM tester with a Berkovich diamond tip. A maximum force of 8 mN was applied to not exceed 10% of the coatings' thickness. For this load at least 8 measurements were made.

Young's modulus E was calculated based on the results obtained, as well as the corresponding standard deviations. The measurement results enabled determination of the H/E as the plasticity index or load factor, which is responsible for the maximum elastic deflection, when the coating is not destroyed and the H^3/E^2 as a resistance to plastic deformation, which determines the load capacity of the coating.

To determine the K_{IC}, a 350 mN normal force was used for each coating to initiate cracks at the indentation sites. The cracks were documented via scanning electron microscopy. The lengths of the cracks were measured and based on the Laugier model formula (Eq. 2) [28], the value of K_{IC} was determined:

$$K_{IC} = x_v \cdot \left(\frac{a}{l}\right)^{\frac{1}{2}} \cdot \left(\frac{E}{H}\right)^{\frac{2}{3}} \cdot \frac{P}{c^{\frac{3}{2}}} \tag{3}$$

where K_{IC}—fracture toughness (MPa·m$^{1/2}$); x_v—indenter geometry factor (for Laugier Equation $x_v = 0.016$); E—Young modulus of the coating (GPa); H—hardness of the coating (GPa); P—the indentation load (mN); a—the length from the center to the corner of the indent (μm); l—the length of the cracks (μm), $c = l + a$, the total length from the center of the indent to the end of crack (μm).

Scratch tests were performed using a MicroCombiTester. They were conducted using a Rockwell indenter with a tip angle of 120°. The scratch length was set at 5 mm with the indenter moving at a constant speed of 5 mm/min, and a normal load linear increase from 1 to 30 N.

3 Results and discussion

3.1 Influence of Cr on the phase structure

GI-XRD was performed on the fabricated coating at an angle of 3°, for which the penetration depth of the X-rays was calculated to be 1.2 μm. Consequently, peaks originating from the substrate were found in the diffraction pattern at $2\theta = 64.7°$ and 82.2°.

The remaining peaks were assigned to the coating material, i.e., a hexagonal TiB_2 phase (pattern number 04-002-5184) and a $TiB_{1.94}$ phase (pattern number 04-001-9272). The presence of a non-stoichiometric phase is visible at $2\theta = 28.16°$ as a peak broadening for the (100) TiB_2 phase. The boron deficiency may be due to its segregation into nanocolumnar grain boundaries during deposition and forming phases with Cr, but the quantity is insufficient to be identified by means of XRD. A second possibility is the simultaneous formation of a B-rich amorphous phase separating stoichiometric TiB_2 nanocolumn structures. Thörnberg et al. [29] identified tightly packed TiB_2 nanocolumnar structures with planar defects of Ti-enriched stacking faults,

accommodating the B deficiency. With the increase in Cr doping, an increase in $TiB_{1.94}$ phase content was observed. All peaks of the TiB_2 phase shifted by 0.2° to the right with increasing Cr doping. Changes in the diffraction angle are a consequence of the modification of interplanar distances in the crystal structure. This indicates the replacement of Ti by Cr. The same or a similar effect was observed in TiB_2 doped with Si, Ta and W [19]. Furthermore, Newirkowez et al. [30] observed the solid solution of transition metals within the (Ti, W, Cr) B coating. From the XRD results, it was observed that the Cr doping induced a change in the preferred orientation of the deposited coatings. The preferred orientation for coatings $Ti_{1-x}Cr_xB_2$ ($x=0$; 0.03; 0.06) was (111) at $2\theta=68.3°$. However, the coating with the highest Cr content was characterized by (101) orientation texturing. Additionally, it was found that chromium doping also affected crystallite size. These values were calculated using the Scherrer equation for grains belonging to the (111) crystallographic orientation. For the undoped coating the grain size was estimated to be 27 nm, while with increasing Cr content, the size decreased to 20 nm and 10 nm for $Ti_{0.97}Cr_{0.03}B_2$ and $Ti_{0.94}Cr_{0.06}B_2$, respectively. It was not possible to determine the crystalline size for $Ti_{0.9}Cr_{0.1}B_2$ coating due to the presence of only one strong (101) peak.

These results clearly show that the addition of Cr to TiB_2 influences the basic interactions between dopants (defects) and surface/grain boundaries (GB). These relations may simply affect the energy balance leading to subsequent stabilization of nanostructures of coating [31]. Therefore, under the same deposition conditions, there are more surface/grain boundaries which have a clear effect on reducing the grain size in the coating material (Fig. 1).

X-ray photoelectron spectroscopy (XPS) coupled with argon ion sputtering was applied to obtain an elemental distribution and to identify the chemical states across the coatings' thickness. The spectral lines B 1*s*, Ti 2*p*, Cr $2p_{3/2}$ (coating material), and Fe $2p_{3/2}$ (steel substrate) were analyzed. Additionally, C 1*s* and O 1*s* lines were identified on the coatings' surface as organic contaminations. Firstly, the surface of each sample was analyzed, followed by measurements performed after every 20 min of argon ion sputtering until reaching the steel substrate. The change in chemical composition for each sample as a function of sputtering time is shown in Fig. 2. The thickness scale is not presented as the Ar ion sputtering rate was not determined. It can be seen that the elements were uniformly distributed across the coatings' thickness, with an increased Cr content near the steel substrate resulting from the Cr interlayer.

The interlayer Cr was observed after different sputtering durations (Fig. 2 a—200 min, b—120 min, c—140 min, 2d—120 min) due to the different sputtering rate.

Figure 3 presents the O 1*s* and Ti 2*p* XPS spectral lines gathered from the coating's surface. The presence of oxygen

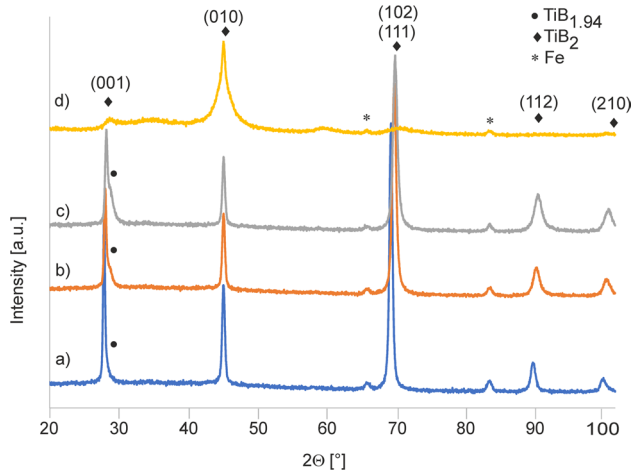

Fig. 1 XRD patterns of $Ti_{1-x}Cr_xB_2$ coatings **a** $x=0$, **b** $x=0.03$, **c** $x=0.06$ and **d** $x=0.1$

O1s is a consequence of the adsorption of contaminants from the environment, forming the oxides layer on the surface. The O 1*s* oxygen line consists of two peaks. The first one at 531 eV is typical for the C=O type bond (contaminations). The second one observed at a higher binding energy (BD) value of 533 eV indicates the presence of organic bonding H–O–C on the coating's surface. The position of the Ti $2p_{3/2}$ peak at 454.5 eV indicates that this is metallic Ti, but we see also satellite or TiO (Ti(2)) as a passivation layer [32]. Peaks resulting from the contaminations layer disappear after the first cycle of sputtering. The XPS spectra of the $Ti_{1-x}Cr_xB_2$ coatings ($x=0.03$, 0.06, 0.1) after 100 min of Ar ion sputtering are presented in Figs. 4, 5 and 6.

The Ti $2p_{3/2}$ and Ti2 $p_{1/2}$ peaks located at binding energies 454.5 eV and 460.5 eV, respectively, are due to the presence of Ti bonded to B in TiB_2 [32]. A small content of TiO was detected at BE = 456.4 eV (Fig. 4). The binding energy of B 1*s* at 187.5 eV results from the metallic state of boron in TiB_2 [33]. Two peaks were identified within the Cr 2*p* spectral line. The binding energy of 574.3 eV is typical for the metallic state of chromium. The second peak at BE = 576 eV (Figs. 4, 5, 6) is typical for Cr on + 3 oxidation state.

Microstructural analysis of pure and Cr-doped TiB_2 coatings was performed via TEM. The thickness of the observed coatings (Fig. 7a–d) varied depending on the Cr interlayer and was estimated to be 1.8 µm, 1.2 µm, 1.4 µm and 1.5 µm for $Ti_{1-x}Cr_xB_2$ ($x=0$; 0.03; 0.06; 0.1), respectively. A columnar crystalline structure was detected in all the coatings. Additionally, it was found that the column width was influenced by the Cr content in the coatings and was in the range of 79 ÷ 30 nm for pure TiB_2, 30 ÷ 23 nm, 50 ÷ 20 nm and 23 ÷ 17 nm for coatings containing $Ti_{1-x}Cr_xB_2$ ($x=0.03$, 0.06, 0.1), respectively. Hexagonal close-packed (hcp) TiB_2 phase was identified in all

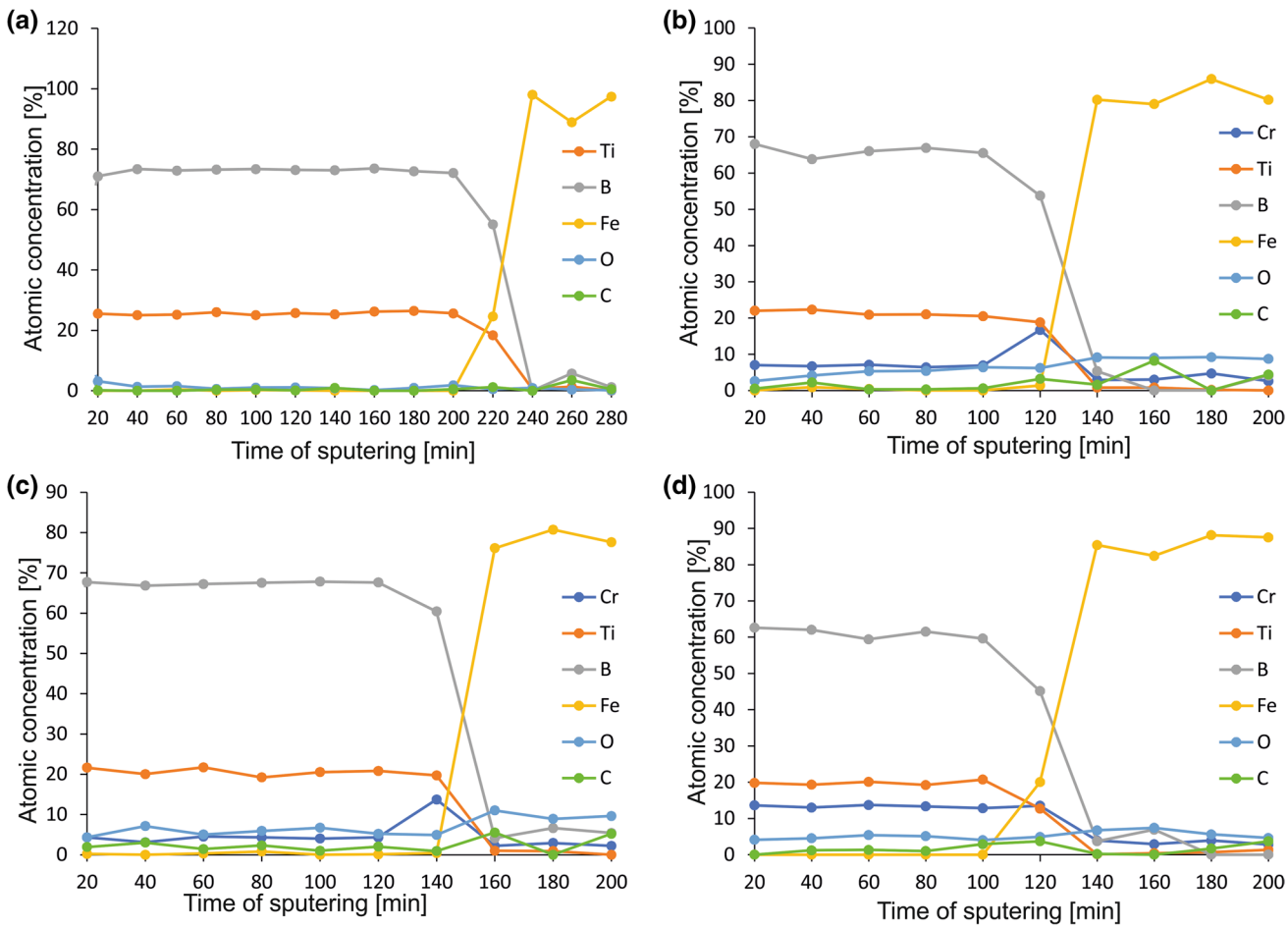

Fig. 2 Atomic concentration depth profiles for coatings $Ti_{1-x}Cr_xB_2$: **a** $x=0$; **b** $x=0.03$; **c** $x=0.06$ and **d** $x=0.1$, obtained using XPS coupled with Ar ion sputtering

coatings. SAED patterns of the $Ti_{1-x}Cr_xB_2$ coatings ($x=0$; 0.03; 0.06) determined the coatings to be monocrystalline (SAED patterns marked as $1 \div 3$ in Fig. 7); however, the diffraction spots were stretched. In contrast, the diffraction pattern of the $Ti_{0.9}Cr_{0.1}B_2$ coating (SAED pattern 4 in Fig. 7) was in the form of continuous rings, which was linked to the doped coating's narrow column widths. Similar results have been previously obtained for Ni-doped [17] and W-doped [19] TiB_2 coatings. Reducing the column widths in TiB_2 coatings with higher chromium content can significantly affect the properties of these materials. An amorphous transition layer of Cr about 400 nm in the pure TiB_2 coating, as well as about 275 nm in the $Ti_{1-x}Cr_xB_2$ ($x=0.03$; 0.06) and 260 nm in the $Ti_{1-x}Cr_xB_2$ ($x=0.1$) are present between the coating and the substrate material. The purpose in depositing this layer was to change the residual stress between the TiB_2 coating and the steel substrate which influence the adhesion of the TiB_2 coating to the substrate. This kind of intermediate layer was previously applied by Berger et al. [5] between a TiB_2 coating and a cemented carbide substrate. He explained that this kind of amorphous or nanocomposite interlayer can be formed when the energy and mobility of the adsorbed atoms is insufficient, as it is in the case of low bias and low substrate temperature. Also, Lofaj et al. [34] in a pure TiB_2 coating magnetron sputtered onto austenitic stainless steel applied amorphous intermediate layer and explained its formation by the gradual evolution of the sputtering parameters, such as low substrate temperature during the initial deposition stage.

The surface topography of the $Ti_{1-x}Cr_xB_2$ coatings was analyzed using atomic force microscopy (AFM) in tapping mode by performing 500×500 nm^2 area scans (Fig. 8), and the results are summarized in Table 1. The topography of all samples is typical for coatings with a columnar structure deposited by physical vapor deposition techniques [31]. In general, they have a very homogeneous and well-developed structure with no surface defects. The roughness varies slightly with the concentration of Cr up

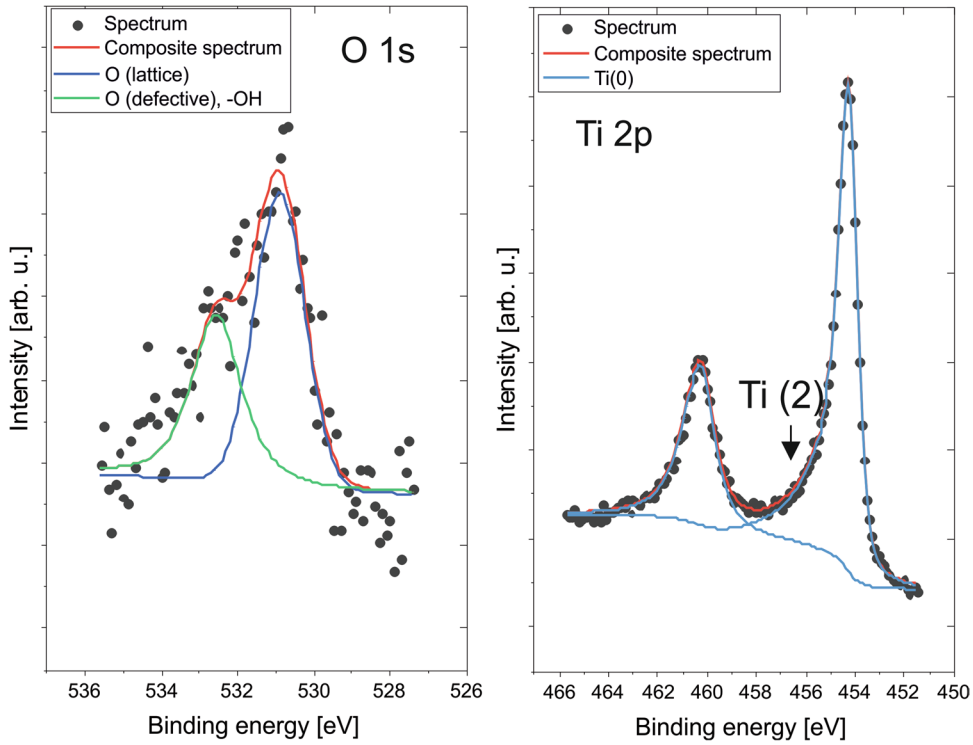

Fig. 3 XPS spectra of O1s, C1*s* and Ti 2*p* obtained from the surface of the TiB_2 coating

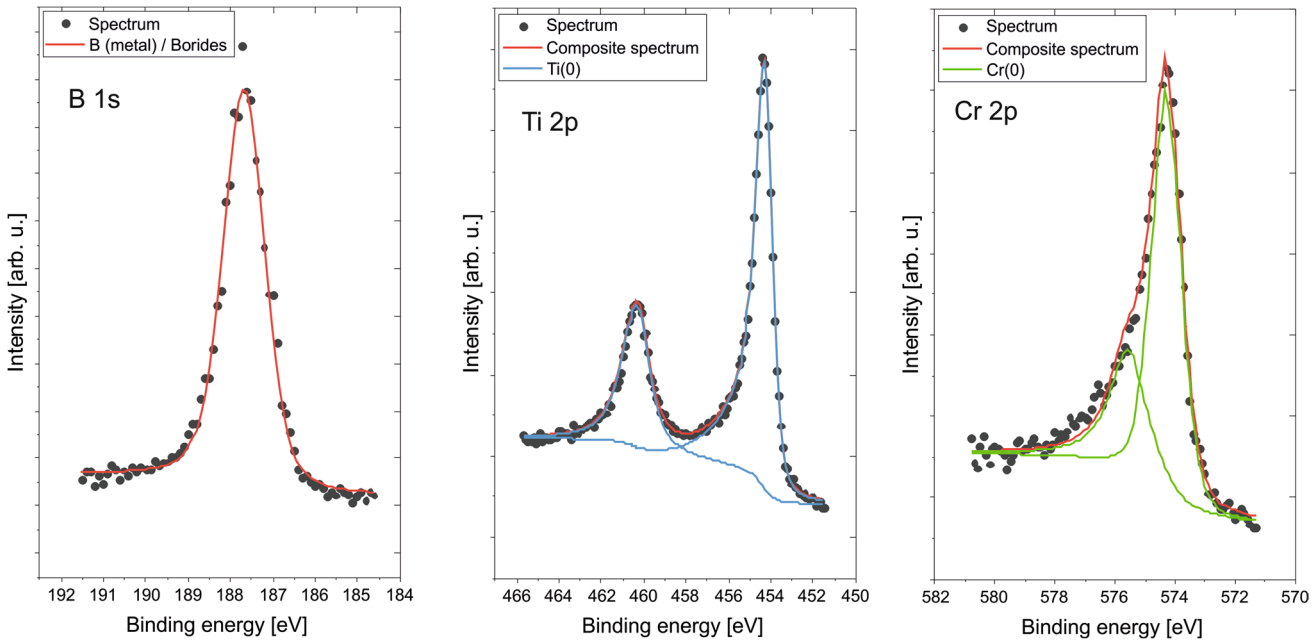

Fig. 4 XPS spectra of B 1*s*, Ti 2*p* and Cr $2p_{3/2}$ of coating $Ti_{0.97}Cr_{0.03}B_2$ after 100 min of sputtering

to 6 at%. For the $Ti_{0.9}Cr_{0.1}B_2$ coating, the R_a parameter was found to be slightly higher. The increase of this value can be explained by the previously discussed change in preferred growth orientation and crystallite size.

3.2 Influence of Cr on mechanical properties

Based on Olivier and Pharr's method and obtained load–displacement curves, the hardness (*H*), Young's modulus (*E*) and their squares were calculated. The results are presented

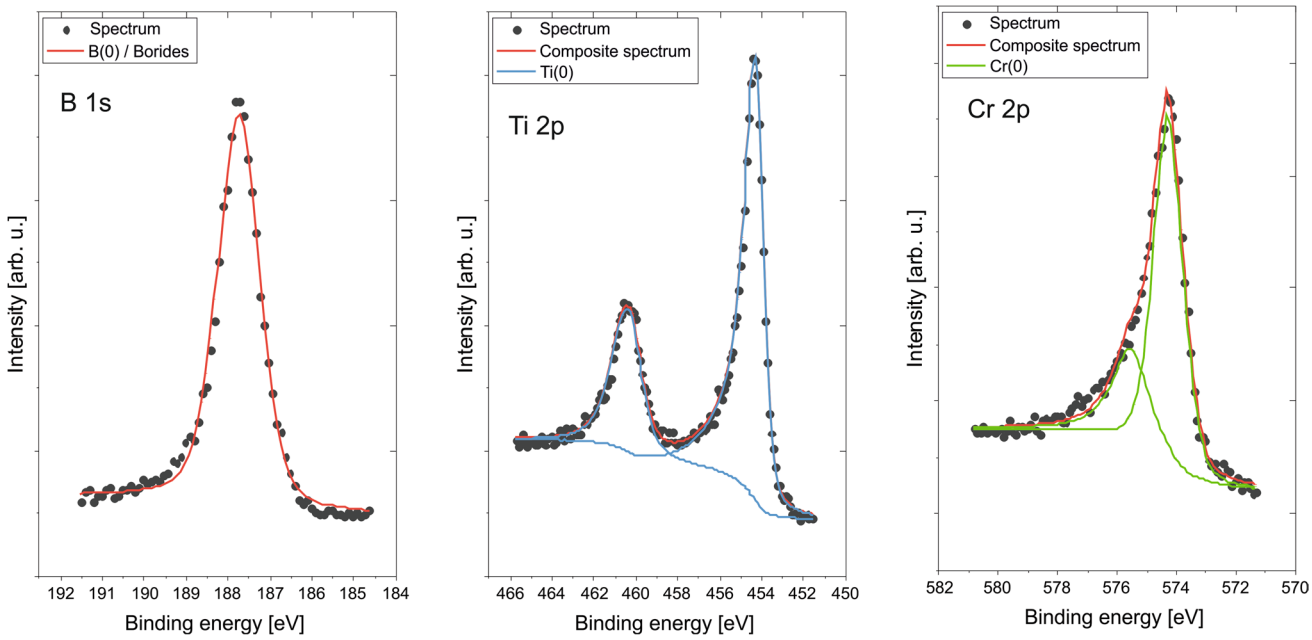

Fig. 5 XPS spectra of B 1*s*, Ti 2*p* and Cr $2p_{3/2}$ of coating $Ti_{0.94}Cr_{0.6}B_2$ after 100 min of sputtering

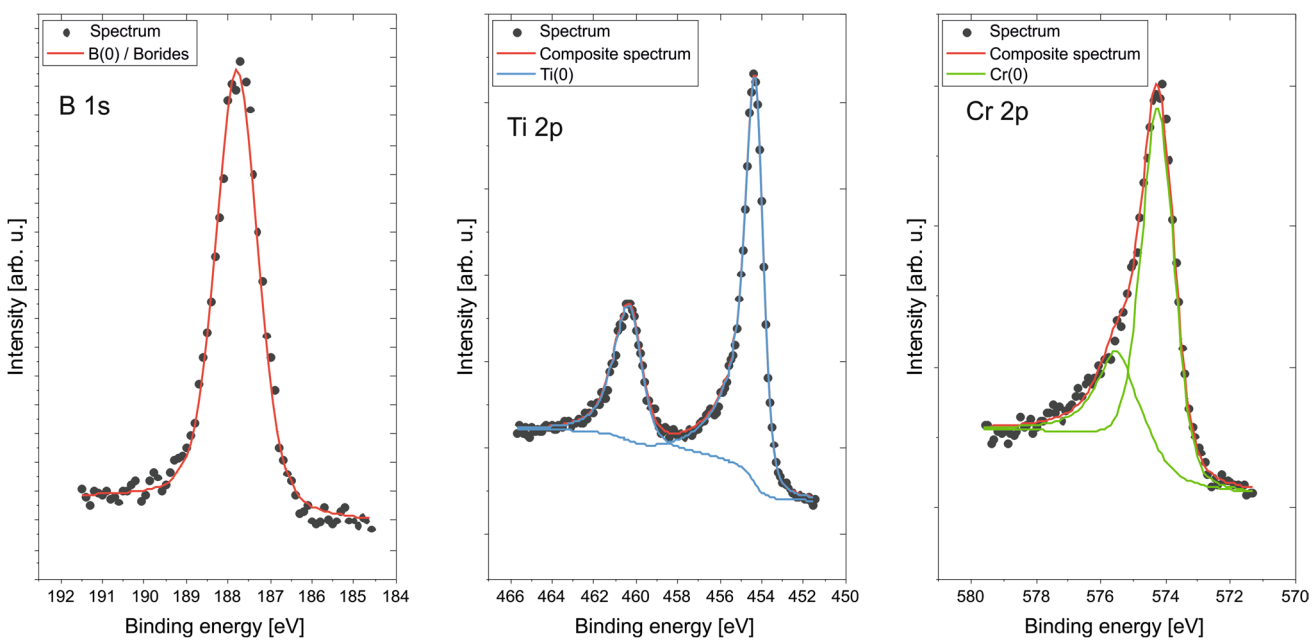

Fig. 6 XPS spectra of B 1*s*, Ti 2*p* and Cr $2p_{3/2}$ of coating $Ti_{0.9}Cr_{0.1}B_2$ after 100 min of sputtering

in Fig. 9 and summarized in Table 2. The hardness and Young's modulus measurements were carried out without exceeding a penetration depth of approx. 9% of the coatings' thickness (max. 90 nm).

The hardness of the pure TiB_2 coating was 37.7 GPa, which is higher than what has been previously reported in the literature [11, 18]. Cr doping affected the material's hardness, firstly by increasing it to 38.5 GPa (maximum value) with 3% at. Cr, and later decreasing it to 35.9 and 36.3 GPa for 6 and 10% at. Cr, respectively. A slight decrease in Young's Modulus with increasing Cr content was registered. Changes in hardness and Young's Modulus were previously observed in coatings doped by Si or W [11, 19]. Several factors can contribute to this. One of them is the preferred

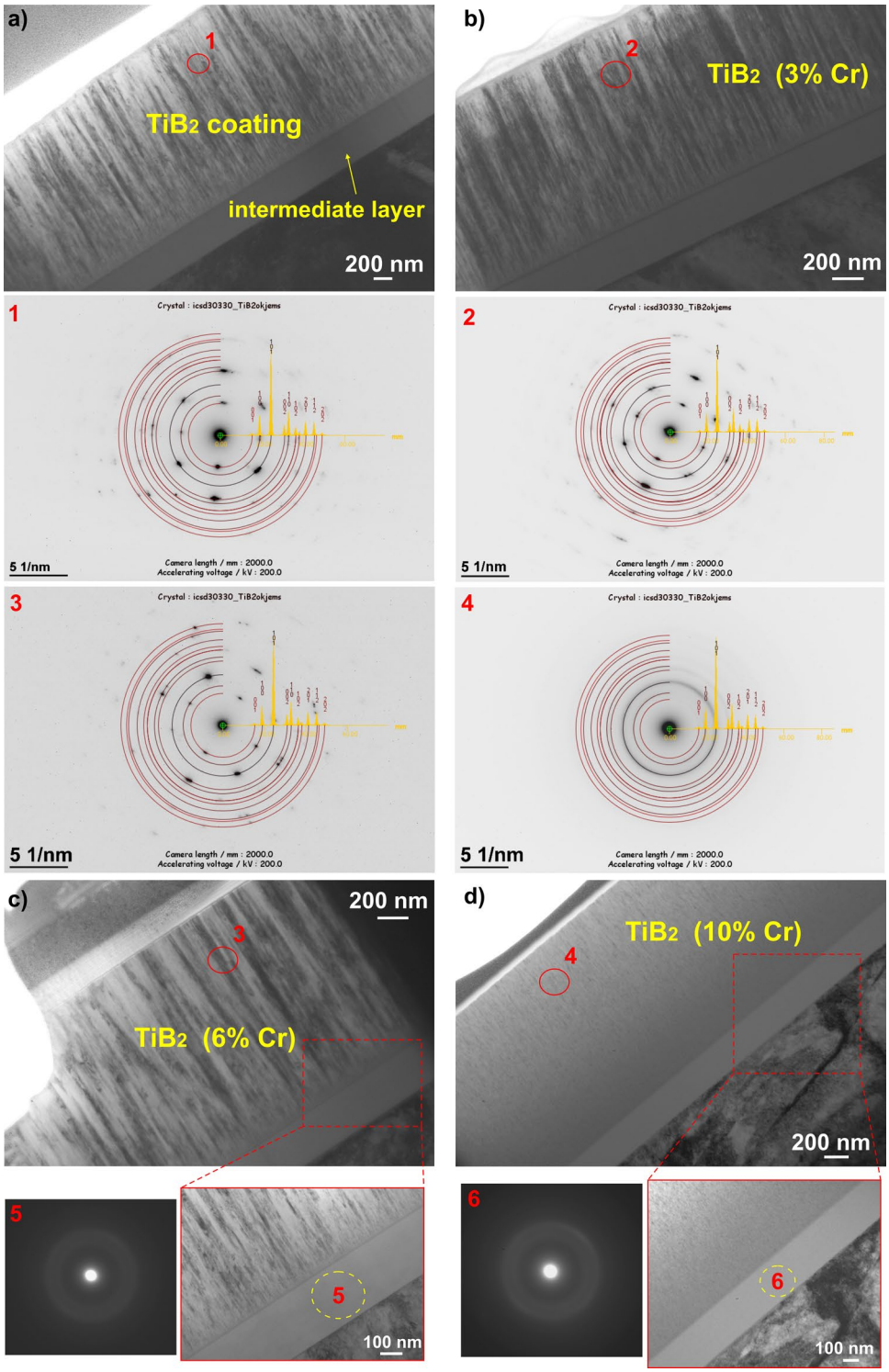

Fig. 7 Cross-sectional TEM micrographs of $Ti_{1-x}Cr_xB_2$ coatings deposited onto steel substrates: **a** $x=0$, **b** $x=0.03$, **c** $x=0.06$ and **d** $x=0.1$; SAED patterns taken from the coating areas marked with numbers 1–4 identified as TiB_2 (hcp) and SAED patterns from intermediate layers marked as 5 and 6

crystallographic orientation of the fabricated coatings. TiB_2 coatings with a (001) orientation are known to yield the highest hardness compared to other TiB_2 coatings with a different orientation [29]. The second cause is due to residual stresses generated in the coating. As the residual stresses increase, the hardness of TiB_2 coatings also increases [34]. Another cause of increased hardness can result from the appearance of nanometric grains or an amorphous phase rich with B. Nanometric grains can impede dislocation generation and motion, and the amorphous phase can inhibit slip at grain boundaries [11]. The last factor may be the presence of a non-stoichiometric boron poor $TiB_{1.94}$ phase, which

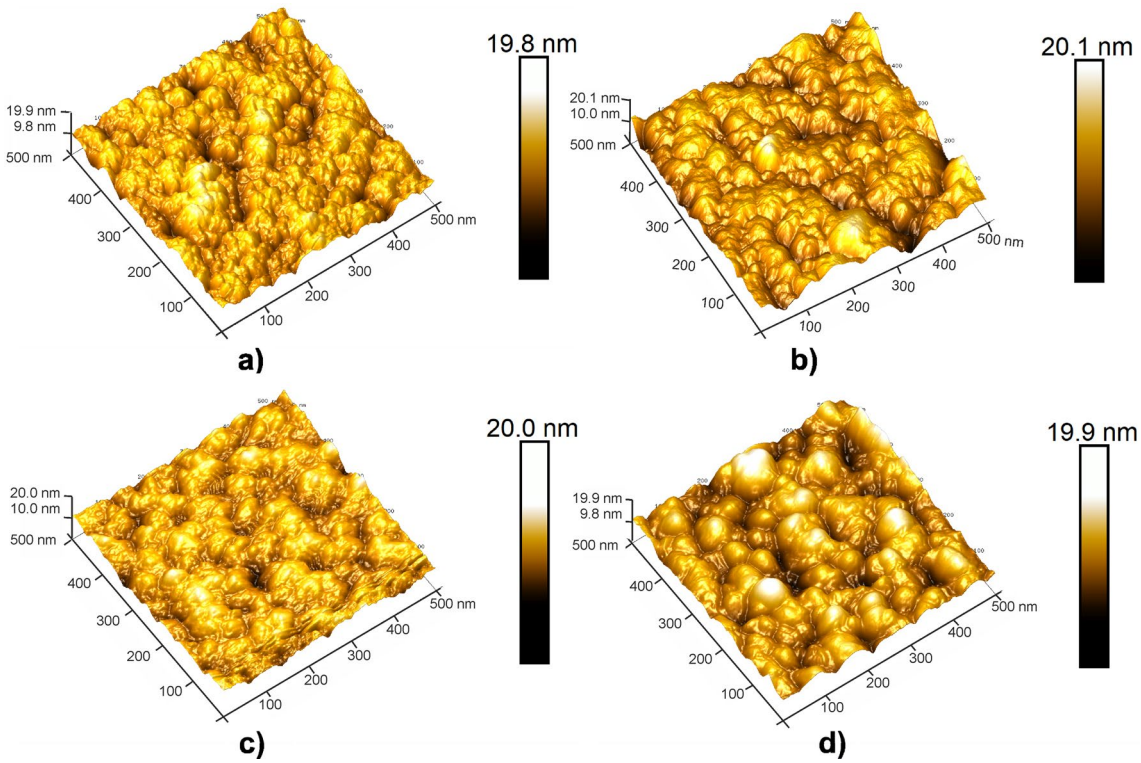

Fig. 8 AFM surface topography for coatings $Ti_{1-x}Cr_xB_2$: **a** $x=0$; **b** $x=0.03$; **c** $x=0.06$ and **d** $x=0.1$

Table 1 Roughness parameters of coatings determined by AFM

Coating	R_a (nm)	R_{max} (nm)
TiB_2	1.14	10.9
$Ti_{0.97}Cr_{0.03}B_2$	1.11	11.3
$Ti_{0.94}Cr_{0.06}B_2$	0.82	7.8
$Ti_{0.9}Cr_{0.1}B_2$	1.60	14.3

Table 2 Mechanical properties of the $Ti_{1-x}Cr_xB_2$ coatings

Coating	H (Gpa)	E (Gpa)	H/E	H^3/E^2	K_{IC} (MPa · m$^{1/2}$)
TiB_2	37.7 ± 1.0	408 ± 13	0.092	0.319	1.88
$Ti_{0.97}Cr_{0.03}B_2$	38.4 ± 2.6	402 ± 15	0.095	0.350	2.66
$Ti_{0.94}Cr_{0.06}B_2$	35.9 ± 1.7	397 ± 13	0.090	0.293	4.36
$Ti_{0.9}Cr_{0.1}B_2$	36.3 ± 1.8	398 ± 21	0.091	0.301	8.5

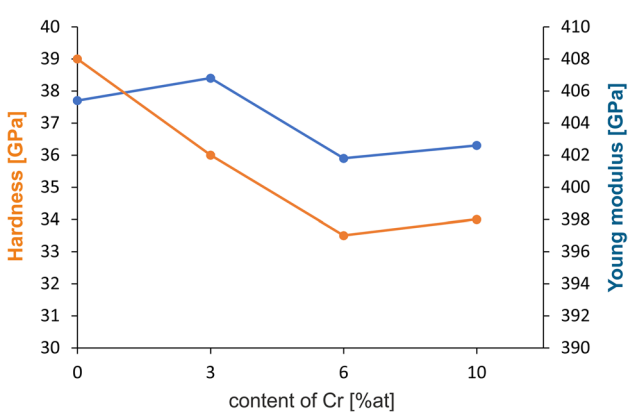

Fig. 9 Hardness and indentation modulus of coatings $Ti_{1-x}Cr_xB_2$ **a** $x=0$; **b** $x=0.03$; **c** $x=0.06$ and **d** $x=0.1$

has a higher hardness than stoichiometric TiB_2 [29]. In all the mentioned potential causes of higher hardness for the $Ti_{0.97}Cr_{0.03}B_2$ coating is the growing volume fraction of the B tissue phase around the TiB_2 grains in overstoichiometric $TiB_{1.94}$. For coating with higher contents of Cr ($x=0.06$; 0.1) the hardness decreases. In these coatings, we observed an increase in the non-stoichiometric phase but also a change in the preferred orientation and a decrease the width of the columns. So, in these coatings grain size and texture are another mechanism that play a more major role, than those seen in the $Ti_{0.97}Cr_{0.03}B_2$ coating.

The resistance of the coating to elastic deformation can be determined by the plasticity index H/E. The H^3/E^2 ratio permits estimation of the material's ability to dissipate energy as plastic deformation during loading. When the H/E ratio is greater than 0.1, the coatings exhibit high

elastic deformation on contact and can be applied where both wear resistance and flexibility are required [35]. For the studied coatings, the obtained H/E values depend on the Cr content. For the $Ti_{0.97}Cr_{0.03}B_2$ coating the H/E value is higher than for the rest of the coating. A coating with a larger H/E is less likely to deform plastically at a given stress and hence should have higher toughness [36] In this coating, the hardness is highest. The H^3/E^2 value of also higher in the $Ti_{0.97}Cr_{0.03}B_2$ coating. Chen X. [36] show that a coating with a larger H^3/E^2 is less likely to be plastically deformed and should therefore have higher toughness.

Next, the materials' fracture toughness (K_{IC}) was determined by measuring the length of the indentation (Berkovich tip) cracks (Fig. 10) made on each coating at a load of 350 mN. Analysis, based on the Laugier model, showed the presence of radial and circular cracks around the indentation marks in all studied coatings. The circular cracks seen related to the increased hardness of the coatings. The presence of radial cracks suggests a tendency towards brittle fractures. The calculated fracture toughness values (K_{IC}) are presented in Table 2. As the Cr content increases, the fracture toughness (K_{IC}) increases from 1.88 to 8.5 MPa $m^{1/2}$. This indicates an apparent increase in the ductility of the coatings.

This effect can be explained by changes in the microstructure of the coatings with increased chromium content. The presence of a non-stoichiometric $TiB_{1.94}$ phase or an amorphous phase can greatly increase the K_{IC} value [29]. The generation of a non-stoichiometric $TiB_{1.94}$ phase (with a lack of B atoms) is a consequence of boron migration and the formation of a boron-enriched amorphous phase separating the stoichiometric TiB_2 nanocolumn structures. Another explanation may be the nanocolumnar structure of the coating. When the width of columns decreases the direction of crack propagation is changed. The energy of a crack is reduced, and cracks may disappear [23].

Scratch testing was performed to evaluate the adhesion of the hard coatings to the substrate. Figure 11 shows the scratch tracks for critical and maximum loads performed on the $Ti_{1-x}Cr_xB_2$ ($x=0$; 0.03; 0.06; 0.1) coatings, respectively. The surface of each mark after the scratch test was observed using an optical microscope (OM) (Fig. 11). For all investigated samples, three scratches were made up to a maximum load of 30 N. For the TiB_2 coating, the first cohesive cracks appeared at a load of 2.4 N (Fig. 11a) and an increase in the load (to 5.6 N) caused the intensification of the cracking process along with the generation of scratch track fragments (Fig. 11a). For the coating with an addition of 3% at. Cr (characterized by the highest hardness), the first cohesive cracks appeared at a lower load 1.8 N (Fig. 11c). The destruction process was similar to that of the TiB_2 coating. For the other coatings, the load at which cohesive cracks appeared increased to 3 N, as seen for $Ti_{0.9}Cr_{0.1}B_2$ (Fig. 11g). For all coatings, increasing the load to a maximum value of 30 N did not result in complete coating detachment, which clearly indicates very good adhesion

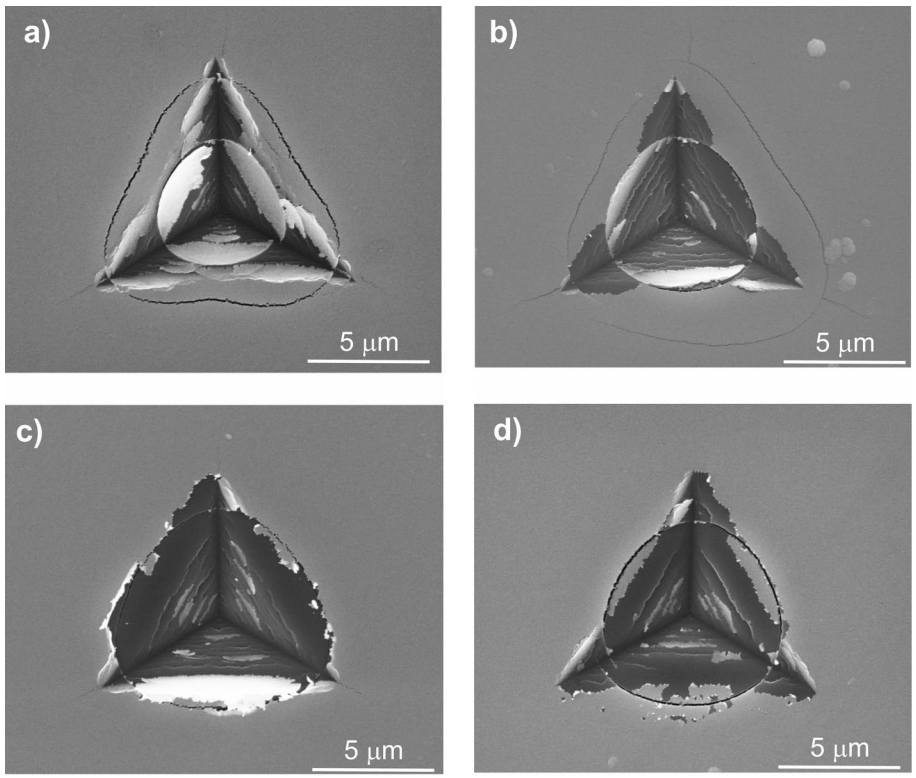

Fig. 10 SEM images of indentation marks obtained for $Ti_{1-x}Cr_xB_2$: **a** $x=0$; **b** $x=0.03$; **c** $x=0.06$ and **d** $x=0.1$

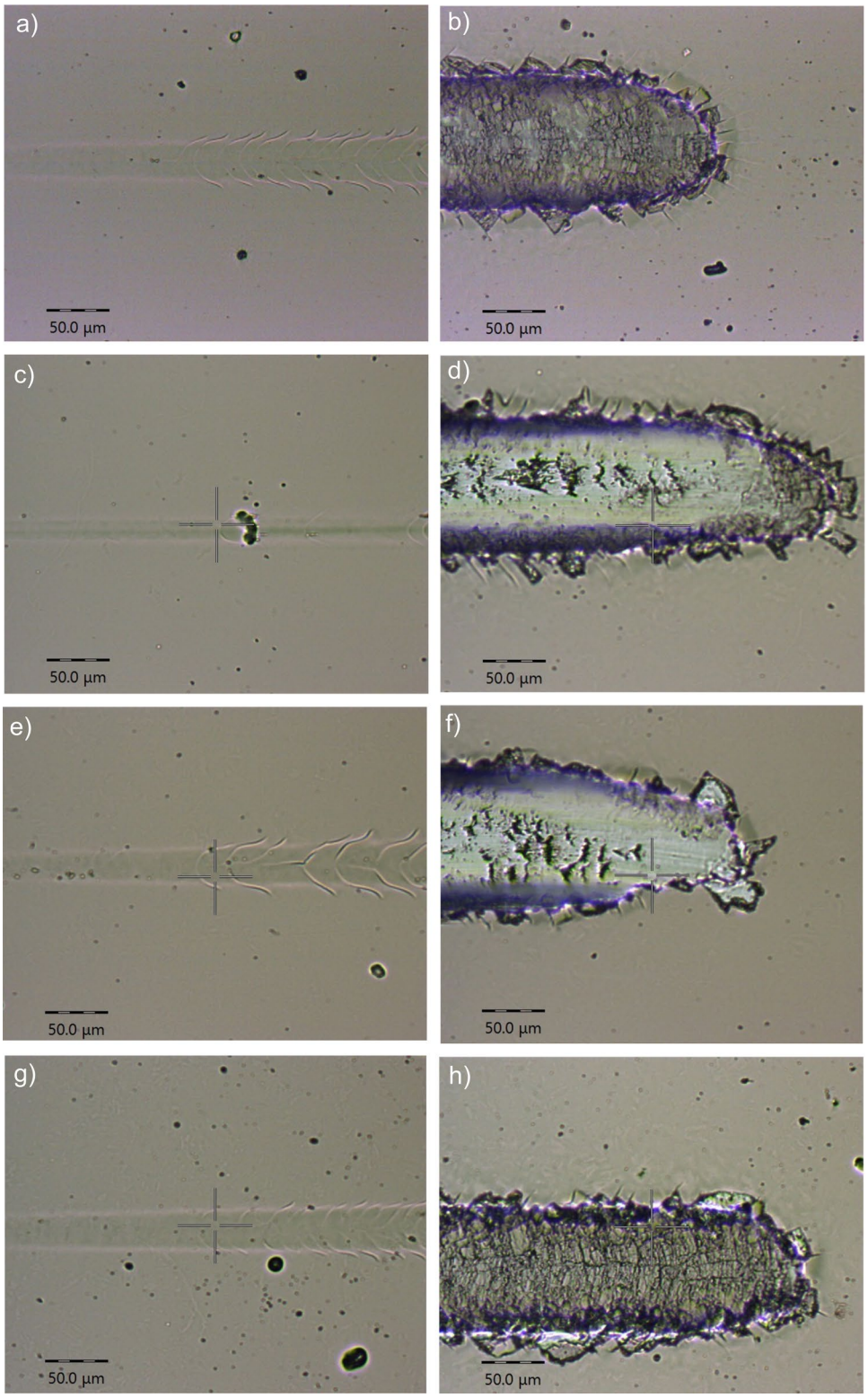

Fig. 11 Scratch tracks images for critical (L_{c1}) and maximum load ($L_{max}=30$ N) of $Ti_{1-x}Cr_xB_2$ coatings: a, **b** $x=0$; **c**, **d** $x=0.03$; **e**, **f** $x=0.06$; **g**, **h** $x=0.1$, respectively

to the substrate. (Fig. 11b, d, f, h). The estimated critical load value L_{c1} in this case is much higher than that observed for the Ti–B–C coating without adhesive layers in reference [31]. It is also higher than that of the TiB_2 coating with a Ti adhesion layer [9], where the L_y force value for the best coating variant was only 0.86 N. Therefore, it can be clearly stated that the application of a pure Cr adhesion layer and

a change in the microstructure of the coatings significantly increased the adhesion of the coatings to the substrate.

4 Conclusions

In this work, the mechanical properties and adhesion of magnetron sputtered Cr-doped TiB_2 coatings with an Cr buffer layer were studied. All $Ti_{1-x}Cr_xB_2$ ($x = 0$; 0.03; 0.06; 0.1) coatings were characterized by homogeneous nanocolumnar structures, and the thickness of the coatings were in the range of $1.2 \div 1.8$ µm. The width of the columns (crystallites) decreased with increasing chromium content (from $27 \div 10$ nm) and XRD phase analysis for all coatings identified two dominant phases: TiB_2 and $TiB_{1.94}$. With the Cr doping content, the texture of the films also changed. These differences in structure strongly influenced the properties of the coatings. The addition of chromium in the TiB_2 coating resulted in a decreased hardness and Young's modulus and an increased fracture toughness (K_{IC}), except for $Ti_{0.97}Cr_{0.03}B_2$. In this coating, the high hardness and reduced adhesion can be explained by the contribution of a non-stoichiometric $TiB_{1.94}$ phase with a hardness increase compared to TiB_2. As the Cr content increases, the volume of $TiB_{1.94}$ increases; however, the column width (crystallite size) decreases simultaneously and the texture changes. These two effects have a significant impact on improving fracture toughness.

Acknowledgements This research was supported by the program "Excellence initiative—research university" for the University of Science and Technology.

Data availability All data generated or analysed during this study are included in this published article.

References

1. Koszela W, Pawlus P, Reizer R, Liskiewicz T. The combined effect of surface texturing and DLC coating on the functionalproperties of internal combustion engines. Tribol Int. 2008;127:470–7. https://doi.org/10.1016/j.triboint.2018.06.034.
2. Cernuschi F, Bison P, Mack DE, Merlini M, Boldrini S, Marchionna S, Capelli S, Concari S, Famengo A, Moscatelli A, Stamm W. Thermo-physical properties of as deposited and aged thermal barrier coatings (TBC) for gas turbines: state-of-the art and advanced TBCs. J Eur Ceram Soc. 2018;38(11):3945–61. https://doi.org/10.1016/j.jeurceramsoc.2018.04.044.
3. Vereschaka A, Aksenenko A, Sitnikov N, Migranov M, Shevchenko S, Sotova C, Batako A, Andreev N. Effect of adhesion and tribological properties of modified composite nanostructured multi-layer nitride coatings on WC-Co tools life. Tribol Int. 2018;128:313–27. https://doi.org/10.1016/j.triboint.2018.07.039.
4. Munro RG. Material properties of titanium diboride. J Res Natl Inst Stand Technol. 2000;105:709–20. https://doi.org/10.6028/jres.105.057.
5. Berger M, Coronel E, Olsson E. Microstructure of d.c. magnetron sputter TiB_2 coatings. Surf Coat Technol. 2004;185:240–4. https://doi.org/10.1016/j.surfcoat.2003.12.029.
6. Kullmer R, Lugmair C, Figueras A, Bassas J, Stoiber M, Mitterer C. Microstructure, mechanical and tribological properties of PACVD Ti(B, N) and TiB_2 coatings. Surf Coat Technol. 2003;1229:174–5. https://doi.org/10.1016/s0257-8972(03)00532-2.
7. Smolik J, Mazurkiewicz A, Garbacz H, Kopia A. Tungsten doped TiB_2 coatings obtained by magnetron sputtering. J Mach Constr Maint. 2018;4:27–32.
8. Lubas J. Assessment and application of TiB_2 coating in sliding pair under lubrication conditions. Wear. 2012;296:504–9. https://doi.org/10.1016/j.wear.2012.08.005.
9. Panjan P, Drnovšek A, Kovač J. Tribological aspects related to the morphology of PVD hard coatings. Surf Coat Technol. 2018;343:138–47. https://doi.org/10.1016/j.surfcoat.2017.09.084.
10. Panich N, Wangyao P, Visuttipitukul P, Sricharoenchai P, Sun Y. Improvement in adhesion of sputtered TiB_2 nano-compostite coatings onto high speed steel by a chromium interlayer. Mater Trans. 2008;49:2331–4. https://doi.org/10.2320/matertrans.MRA2008107.
11. Ye Y, Liu Z, Liu W, Zhang D, Wang Y, Zhao H, Li X. Effect of interlayer design on friction and wear behaviors of CrAlSiN coating under high load in seawater. RSC Adv. 2018;8:5596–607. https://doi.org/10.1039/C7RA12409K.
12. Akhter R, Zhou Z, Xie Z, Munroe P. Enhancing the adhesion strength and wear resistance of nanostructured NiCrN coatings. Appl Surf Sci. 2021;541:148533. https://doi.org/10.1016/j.apsusc.2020.148533.
13. Ali A, Ahmad SN. Mechanical and tribological behavior of TiB_2/Al_2O_3 coating on high-speed steel using electron beam deposition. Trib Intern. 2022;174:107681. https://doi.org/10.1016/j.triboint.2022.107681.
14. Park B, Jung D-H, Kim H, Yoo K-C, Lee J-J, Joo J. Adhesion properties of TiB_2 coatings on nitrided AISI H13 steel. Surf Coat Technol. 2005;200:726–9. https://doi.org/10.1016/j.surfcoat.2005.01.064.
15. Ozkan D. Friction and wear enhancement of magnetron sputtered bilayer Cr–N/TiB_2 thin-film coatings. Wear. 2020;454–455:203344. https://doi.org/10.1016/j.wear.2020.203344.
16. Gruber DP, Zalesak J, Todt J, Tkadletz M, Sartory B, Suuronen J-P, Ziegelwanger T, Czettl C, Mitterer C, Keckes J. Surface oxidation of nanocrystalline CVD TiB_2 hard coatings revealed by cross-sectional nano-analytics and in-situ micro-cantilever testing. Surf Coat Technol. 2020;399:126181. https://doi.org/10.1016/j.surfcoat.2020.126181.
17. Wang H, Wang B, Li S, Xue Q, Huang F. Toughening magnetron sputtered TiB_2 coatings by Ni addition. Surf Coat Technol. 2013;232:767–74. https://doi.org/10.1016/j.surfcoat.2013.06.094.

18. Contreras E, Galindez Y, Gómez MA. Microstructure, mechanical and tribological properties of TiBC coatings by DC magnetron sputtering onto AISI M2 steel using independent TiB_2 and graphite targets. Surf Coat Technol. 2018;350:298–306. https://doi.org/10.1016/j.surfcoat.2018.05.079.
19. Chudzik-Poliszak E, Cieniek Ł, Moskalewicz T, Kowalski K, Kopia A, Smolik J. Influence of W addition on microstructure and resistance to brittle cracking of TiB_2 coatings deposited by DCMS. Materials. 2021;14:4664. https://doi.org/10.3390/ma14164664.
20. Huang X, Sun S, Tu G. Investigation of mechanical properties and oxidation resistance of CVD TiB_2 ceramic coating on molybdenum. J Mat Res Tech. 2020;9(1):282–90. https://doi.org/10.1016/j.jmrt.2019.10.056.
21. Elders J, Quist PA, Rooswijk B, Voorst JDW, Nieuwkoop J. CO_2-laser-induced chemical vapour deposition of TiB_2. Surf Coat Technol. 1991;45:105–13. https://doi.org/10.1142/S0218625X1250045X.
22. Berger M, Larsson M, Hogmark S. Evaluation of magnetron-sputtered TiB_2 intended for tribological applications. Surf Coat Technol. 2000;124:253–61. https://doi.org/10.1016/S0257-8972(99)00638-6.
23. Panich N, Sun Y. Effect of substrate rotation on structure, hardness and adhesion of magnetron sputtered TiB_2 coating on high speed steel. Thin Solid Films. 2006;500:190–6. https://doi.org/10.1016/j.tsf.2005.11.055.
24. Kelesoglu E, Mitteter C. Structure and properties of TiB_2 based coatings prepared by unbalanced DC magnetron sputtering. Surf Coat Technol. 1998;98:1483–9. https://doi.org/10.1016/S0257-8972(97)00397-6.
25. Xu Y, Yamazaki M, Villars P. Inorganic materials database for exploring the nature of material. Jpn J Appl Phys. 2011;50:11RH02. https://doi.org/10.1143/JJAP.50.11RH02.
26. Cybroń J. Residual stress analysis after machining in composite materials based on aluminum alloy with ceramic additive. Mechanik. 2018;1:28–30. https://doi.org/10.17814/mechanik.2018.1.4.
27. Burton AW, Ong K, Rea T, Chan I. On the estimation of average crystallite size of zeolites from the Scherrer equation: a critical evaluation of its application to zeolites with one-dimensional pore systems. Microporous Mesoporous Mater. 2009;117:75–90. https://doi.org/10.1016/j.micromeso.2008.06.010.
28. Smolik J, Kacprzyńska-Gołacka J, Sowa S, Piasek A. The analysis of resistance to brittle cracking of tungsten doped TiB_2 coatings obtained by magnetron sputtering. Coatings. 2020;10:807. https://doi.org/10.3390/coatings10090807.
29. Thornberg J, Palisaitis J, Hellgren N, Klimashin F, Ghafoor N, Zhirkov I, Azina C, et al. Microstructure and materials properties of understoichiometric TiB_x thin films grown by HiPIMS. Surf Coat Technol. 2020;404:126537. https://doi.org/10.1016/j.surfcoat.2020.126537.
30. Newirkowez A, Cappi B, Telle R, Schmidt H. (Ti, W, Cr)B_2 coatings produced by dc magnetron sputtering. Thin Solid Films. 2012;520:1775–8. https://doi.org/10.1016/j.tsf.2011.08.071.
31. Nafsin N, Castro RHR. Direct measurements of quasi-zero grain boundary energies in ceramics. J Mater Res. 2017;32:166–73. https://doi.org/10.1557/jmr.2016.282.
32. Sanchez CMT, Rebollo Plata B, Maia da Costa MEH, Freire FL Jr. Titanium diboride thin films produced by dc-magnetron sputtering: structural and mechanical properties. Surf Coat Technol. 2011;205:3698–702. https://doi.org/10.1016/j.surfcoat.2011.01.014.
33. Güzelçimen F, Tanoren B, Çetinkaya Ç, Donmez M, Efkere HI, Ozen Y, Bingol D, et al. The effect of thickness on surface structure of RF sputtered TiO_2 thin films by XPS, SEM/EDS, AFM and SAM. Vacuum. 2020;182:109766. https://doi.org/10.1016/j.vacuum.2020.109766.
34. Lofaj F, Moskalewicz T, Cempura G, Mikula M, Dusza J, Czyrska-Filemonowicz A. Nanohardness and tribological properties of nc-TiB_2 coatings. J Eur Ceram Soc. 2013;33:2347–53. https://doi.org/10.1016/j.jeurceramsoc.2013.02.024.
35. Charitidis C, Panayiotatos Y, Logothetidis S. A quantitative study of the nano-scratch behavior of boron and carbon nitride films. Diam Relat Mater. 2003;12:1088–92. https://doi.org/10.1016/S0925-9635(02)00268-6.
36. Chen X, Du Y, Chung YW. Commentary on using H/E and $H3/E2$ as proxies for fracture toughness of hard coatings. Thin Solid Films. 2019;688:137265. https://doi.org/10.1016/j.tsf.2019.04.040.